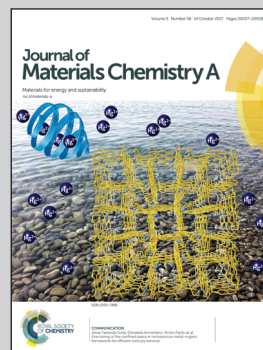


Showcasing a new approach on improving the reactivity of iron oxide oxygen carriers using a very small concentration of the lanthanum dopant by Professor Liang-Shih Fan's research group at the Ohio State University.

Improved cyclic redox reactivity of lanthanum modified iron-based oxygen carriers in carbon monoxide chemical looping combustion

Oxygen carriers are required to have high reactivity and recyclability with low cost. A very low concentration of the lanthanum dopant can dramatically increase the reactivity of oxygen carriers in chemical looping combustion with carbonaceous fuels by reducing the reaction barriers. This methodology provides substantial performance improvements of oxygen carriers that are relatively simple to fabricate, and it will have an impact on chemical looping particle design and modification.

As featured in:



See Liang-Shih Fan et al.,
J. Mater. Chem. A, 2017, 5, 20153.



rsc.li/materials-a

Registered charity number: 207890



Cite this: *J. Mater. Chem. A*, 2017, 5, 20153

Improved cyclic redox reactivity of lanthanum modified iron-based oxygen carriers in carbon monoxide chemical looping combustion

Lang Qin,^{†a} Mengqing Guo,^{†a} Zhuo Cheng,^{†a} Mingyuan Xu,^a Yan Liu,^a Dikai Xu,^a Jonathan A. Fan^b and Liang-Shih Fan^{ID}^{*a}

Chemical looping combustion (CLC) technology converts fuel into heat or electricity with complete CO₂ capture and does not require air separation units. CLC is realized through redox reactions of gas or solid fuels with oxygen carriers at high temperatures. The oxygen carriers are required to have high reactivity and recyclability with low cost. In this work, we use a low concentration of the lanthanum dopant to dramatically change the reactivity of oxygen carriers in CLC with CO fuel. Lanthanum is a rare earth element and is chosen because of its high catalytic activity. It is found that the conversion rates of lanthanum-doped oxygen carriers are universally higher than those of undoped iron oxide oxygen carriers from 550 °C to 780 °C. The reactivity increases significantly in doped oxygen carriers at these temperatures favourable for CLC and decreases in these carriers at temperatures above approximately 800 °C due to enhanced sintering. Density functional theory (DFT) is used to calculate the surface configuration and energy barriers in CLC reactions and shows dramatically reduced energy barriers in lanthanum-doped iron oxide reactions with CO and oxygen carrier regeneration. This methodology provides substantial reactivity improvements of CLC with oxygen carriers that are relatively simple to fabricate, and it will have an impact on chemical looping particle design and modification.

Received 15th May 2017
Accepted 26th June 2017

DOI: 10.1039/c7ta04228k

rsc.li/materials-a

Introduction

Cyclic redox reactions have a variety of applications in clean energy such as photocatalysis, batteries, fuel cells, and chemical looping processes.¹ In a chemical looping combustion (CLC) system, metal oxides react with gas or solid fuels in a reducer and regenerate in an oxidizer. The cycling of these processes can produce heat or electricity with a CO₂ stream that does not contain any nitrogen. This pure CO₂ stream is easy to capture, pressurize, store, and transport. In the conversion of carbonaceous fuels using the CLC technology, CO is produced in the process as an intermediate species. Thus, the reaction between the oxygen carriers and CO is vitally important for the full conversion of the fuel. Consequently, CLC is highly efficient and economical for CO₂ capture, making it one of the most promising technologies in the clean energy industry.² The application of CLC can successfully eliminate the cost of additional energy required by other technologies for carbon dioxide separation

processing. Moreover, NO_x formation in CLC is minimal, which prevents combustion-induced acid rain or smog.³

Oxygen carriers in the CLC process are required to have high reactivity and recyclability, along with low cost and high stability at high temperatures.⁴ Iron oxides with suitable modification have been singled out as one of the most promising oxygen carriers that meet all of these requirements. Intensive efforts have been put into the research and modification of these active oxygen carriers to further enhance their reduction and regeneration reactivity. One strategy has been to introduce a low concentration of catalytic dopants into active oxygen carrier hosts, with the objective of promoting ionic adsorption and diffusion in redox reactions without a reduction in their oxygen carrying capacity.⁵

A number of groups have studied the modification of reactive and support materials in oxygen carriers, for the purposes of increasing recyclability and reactivity.^{6–8} Mohamed *et al.*⁹ demonstrated that the CO conversion rate increases with the addition of 2–10% Ce in a NiO oxygen carrier. Liu *et al.*¹⁰ found that a 5% doping level of an alkali metal in an Fe₂O₃/Al₂O₃ composite stabilizes the reactivity of the oxygen carrier over the course of 50 redox cycles and prevents Fe–Al phase separation in the composite. Wang *et al.*¹¹ investigated 8% Zr-doped Cu-based oxygen carriers for oxyfuel combustion using an O₂–CO₂ mixed gas to effectively capture CO₂ with high concentrations. The

^aDepartment of Chemical and Biomolecular Engineering, The Ohio State University, 140 West 19th Ave, Columbus, OH 43210, USA. E-mail: fan.1@osu.edu

^bDepartment of Electrical Engineering, Ginzton Laboratory, Spilker Engineering and Applied Sciences, Stanford University, 348 Via Pueblo Mall, Stanford, CA 94305, USA

[†] Co-first authors.

combination of density functional theory (DFT) calculations and experiments proved that the addition of Zr increased the oxygen release capability of oxygen carriers with improved cycling stability. Imtiaz *et al.*¹² demonstrated that 40–50% CeO_{2-x}-stabilized CuO oxygen carriers had increased oxygen capacity, coke resistance, and redox stability. Generally, alkali earth metals, transition metals, and rare earth metals have been screened as modifying materials at high concentrations (10–50%) in perovskite materials.^{13,14} These modifications can either change the lattice parameters or crystal phases, impacting the oxygen carrying capacity and reactivity during chemical looping reactions.

The study of low dopant concentrations that do not modify the crystal phases of iron oxide oxygen carriers is of significant importance in maintaining high oxygen capacity with low cost.⁵ However, it is a major challenge to effectively utilize dopants at low concentrations, and it requires a profound understanding of the structure–property relationship of doped oxygen carriers. *Ab initio* DFT+*U* calculations can complement experimental mechanistic studies and provide valuable information on the structure of the active sites and the energy of adsorbed species interacting with the surfaces.^{15,16} In addition, detailed reaction pathways can be derived and characterized by the energy profile of the constituent elementary steps. To the best of our knowledge, using various types of metal oxide modifiers, serving as dopants, promoters or enhancers at very low concentration relative to the total metal oxide oxygen carriers (*e.g.*, <1%) without yielding phase modification, to reduce the energy barrier of carbonaceous feedstock activation on metal oxide materials during the redox process and hence augmentation of the carbonaceous feedstock conversion was first initiated by Qin *et al.*^{5,17,18} In the work of Qin *et al.*,^{5,17} the 1% isovalent dopant, *i.e.*, La, and in the work of Qin *et al.*,¹⁸ the 2% or lower (*e.g.*, 0.5%) aliovalent dopants (*e.g.*, Ni) promoted reactivity of carbonaceous fuels with oxygen carriers were used to demonstrate the effectiveness of low dopant concentration in the enhancement of fuel conversion. No work has been conducted to date on the effect of very low concentration dopants on the adsorption of CO alone and its corresponding oxidation mechanism. The lack of the knowledge of the low concentration dopant effects is hampering the design and development of effective oxygen carriers of low costs.

In this work, we comprehensively investigate the CO reactivity and regeneration reactivity of low concentration La-doped Fe₂O₃ oxygen carriers in a wide CLC temperature window. La₂O₃ has been shown previously to be an effective catalyst for the oxidative coupling of methane (OCM)¹⁹ and CO oxidation.²⁰ The optimal configuration of La dopants at the oxygen carrier surface enables the dopant to actively provide extra reaction sites, as well as lower reaction energy barriers for both CO combustion and oxygen carrier regeneration. The active sites in turn will dramatically increase the reactivity at working CLC temperatures. This work will provide insights into effective oxygen carrier design and modification, and the proposed doped oxygen carriers will enable the lowering of CLC operation temperatures.

Experimental

Sample preparation

La-Doped Fe₂O₃ was made from La₂O₃ (99% purity) and Fe₂O₃ powders (99.99% purity), both were purchased from Fisher Scientific. Fe₂O₃ powder was mixed by ball milling for 24 hours at room temperature with 0.5%, 1%, or 2% La₂O₃ dopant powders. The mixed powders were uniaxially pressed into a pellet with a diameter of 8 mm and a thickness of 2–3 mm. The top surfaces were perpendicular to the pressing direction and parallel to the die surfaces. The samples were heat treated in air at 110 °C for 2 hours to remove volatile impurities using a 2 °C minute^{−1} heating rate and then sintered at 1300 °C for 2 hours using 2 °C minute^{−1} heating and 2 °C minute^{−1} cooling rates, respectively. As a reference, an undoped Fe₂O₃ powder was subject to the same treatment as that of the La-doped samples.

TGA operation

Pellet samples weighing approximately 30 mg were mounted in an alumina crucible, and continuous reduction–regeneration cycles were conducted at six different temperatures between 550 °C and 800 °C using a Setaram SETSYS Evolution Thermogravimetric Analyzer (TGA). The reduction step was performed using a 200 mL minute^{−1} flow of gas containing 20% CO balanced with N₂. The regeneration step was performed using a 320 mL minute^{−1} flow of gas consisting of 50% air balanced with N₂. The reduction and regeneration steps lasted for 15 minutes each and were alternated with an intermediate 5 minute flushing step using N₂ at 160 mL minute^{−1}.

Characterization

The samples were analyzed using a Rigaku SmartLab X-ray Diffractometer (XRD) with a monochromator to eliminate fluorescence generated by iron. Scans were performed at 30–80 degrees at a rate of 0.1 degree per minute with an accelerating voltage and filament current of 40 kV and 44 mA, respectively. All the XRD spectra were analyzed using PDXL software and identified with the JCPDS database. Scanning electron microscope images were obtained with a 20 kV and 43 pA electron beam. A Kratos Axis Ultra DLD spectrometer was used to obtain X-ray photoelectron (XPS) spectra. Mg K α monochromatic X-ray radiation (1253.8 eV) was applied to ensure the optimal peak intensity of La. The spectra were collected at room temperature. Binding energy (B.E.) values were referenced to the standard C 1s binding energy of 284.8 eV. The CasaXPS program was used for data analysis. A Shirley-type background and Lorentzian–Gaussian combination were used for data processing. The spin–orbit splitting in the La 3d region gives rise to a doublet with 3d_{5/2} and 3d_{3/2}. The area ratio for the two spin–orbit peaks is 3 : 2.

Theory

All calculations were performed within the framework of density functional theory (DFT), as implemented in the Vienna

ab initio simulation package (VASP).^{21–23} The generalized gradient approximation of Perdew, Burke and Ernzerhof was used to represent the exchange–correlation energy.²⁴ The projector-augmented wave (PAW) method, with a 400 eV energy cutoff, was used to describe the wave functions of the atomic cores. The $8 \times 8 \times 1$ Monkhorst–Pack k -point mesh was used for surface calculations to obtain results that were converged within 1×10^{-5} eV, using the conjugate gradient method. To study the effect of incorporating La, a single Fe atom was replaced by a La atom in hexagonal unit cells of 240 atoms ($2 \times 4 \times 1$ supercell). The La/Fe ratio corresponds to 1/96, thus mimicking 1% La concentration.

The adsorption energies (E_{ad}) were calculated by the following equation:

$$E_{\text{ad}} = (E_{\text{sur}} + E_{\text{CO}}) - E_{\text{system}}$$

where E_{sur} , E_{CO} and E_{system} are the energies of the clean surface, the isolated CO molecule and the adsorption system, respectively.

For CO activation barrier calculations, the climbing-image nudged elastic band (CI-NEB) method was used. This method enabled the stationary points to be mapped out along the minimum energy paths and identified transition states for each of the diffusion processes. Because these paths were directed by force projection, the energy was not necessarily consistent with the force being optimized; thus, a force-based optimizer was chosen to ensure the convergence of the nudged elastic band algorithm.

Due to the valence electrons of Fe (4s, 3d), O (2s, 2p), C (2s, 2p), and H (1s) states, the Hubbard U approach is used to correct self-interaction errors of $\alpha\text{-Fe}_2\text{O}_3$. The increase of U from 1 eV to 4 eV results in improved values for magnetic moments and the band gap, as well as better agreement with the density of states by experimental inverse photoemission spectra. A further increase in U cannot achieve a better agreement. In addition, the band gap becomes too large and occupied Fe 3d states are shifted to unacceptably low energies, *i.e.*, $U > 4.2$ eV. Therefore, we choose $U = 4$ eV to describe the energy required for adding an extra d electron to an Fe atom.

Results and discussion

The impact of the La dopant on crystal phase modification was studied by XRD. Fig. 1 shows the XRD patterns of rhombohedral Fe_2O_3 (Fig. 1(a)) and 0.5%, 1%, and 2% La-doped Fe_2O_3 (Fig. 1(b) and (c)). No phase of La_2O_3 was detected in all doped samples, indicating complete solid-state reactions between La_2O_3 and Fe_2O_3 . On the other hand, the impurity phase LaFeO_3 is formed in 2% La-doped Fe_2O_3 . This suggests that at concentrations less than 2%, La is completely incorporated into Fe_2O_3 unit cells. To simplify a model for theoretical study, we choose 1% La-doped Fe_2O_3 for CLC reactions in this work.

Chemical surface modifications mediated by the La dopant is analysed by XPS through surface species analysis. As a comparison, the XPS spectra for La and O in undoped and doped Fe_2O_3 are shown in Fig. 2. We note that the Fe spectra are

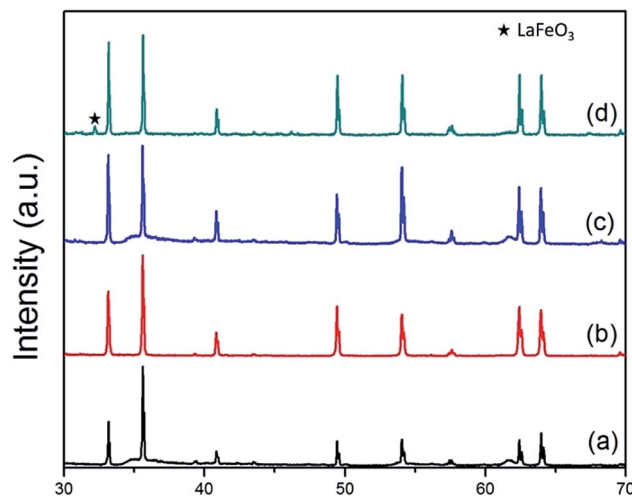


Fig. 1 (a) XRD spectra of (a) Fe_2O_3 , (b) 0.5% La-doped Fe_2O_3 , (c) 1% La-doped Fe_2O_3 and (d) 2% La-doped Fe_2O_3 .

not discussed in this work because a Mg source is used for optimal La spectra detection. The LMM spectra from the Mg source coincidentally overlap with the Fe 2p spectra, which impacts the accuracy of Fe analysis. As expected, no La was detected on the surface of undoped iron oxide (Fig. 2(a)). In La-doped Fe_2O_3 , the La 3d region has well-separated spin-orbit components. In this case, the La 3d spectrum has four visible components.²⁵ As shown in Fig. 2(b), The binding energy values of La $3d_{3/2}$ and La $3d_{5/2}$ (the spin-orbit splitting of La was 16.8 eV) were 834.7 eV and 838.1 eV, respectively, which represent La–O₁ and La–O₂ bonds on the surface. Fig. 2(c) and (d) show the O 1s spectra of undoped and La-doped Fe_2O_3 , respectively. The O 1s peak of undoped iron oxide suggests two species on the pellet surface: Fe–O bond and hydroxyl groups, as illustrated by peaks at 529.6 eV and 532.0 eV, respectively. The latter is unavoidable on the outermost surface of metal oxides.²⁶ In the La-doped sample, three peaks are exhibited at 529.6 eV, 531.1 eV and 532.0 eV, which can be ascribed to an Fe–O bond, La–O bond, and hydroxyl group, respectively. The concentrations of La and O species on the surfaces of undoped iron oxide and La-doped iron oxide are displayed in Table 1. The La/O ratio is 0.054 from XPS detection on the surface of 1% La-doped Fe_2O_3 , which is approximately 8 times higher than the theoretical value of 0.0067 for bulk materials. The higher concentration of La on the surface indicates that La atoms have a tendency to accumulate at surfaces, rather than in the bulk material. This is advantageous in cyclic reactions, as the efficiency of active La sites remains high on the surface.

TGA analysis shows that La-doped Fe_2O_3 has dramatically enhanced conversion rates in CO reduction and oxygen carrier regeneration compared to undoped Fe_2O_3 . Fig. 3 shows typical oxygen carrier conversion rates in 10 continuous reduction and regeneration cycles. The reduction and oxidation reactivity universally increases in both Fe_2O_3 and 1% La-doped Fe_2O_3 oxygen carriers between 550 °C and 750 °C, as illustrated in Fig. 3(a). At 700 °C, the CO reduction conversion rate is maximized in 1% La-doped Fe_2O_3 and is 233% higher than

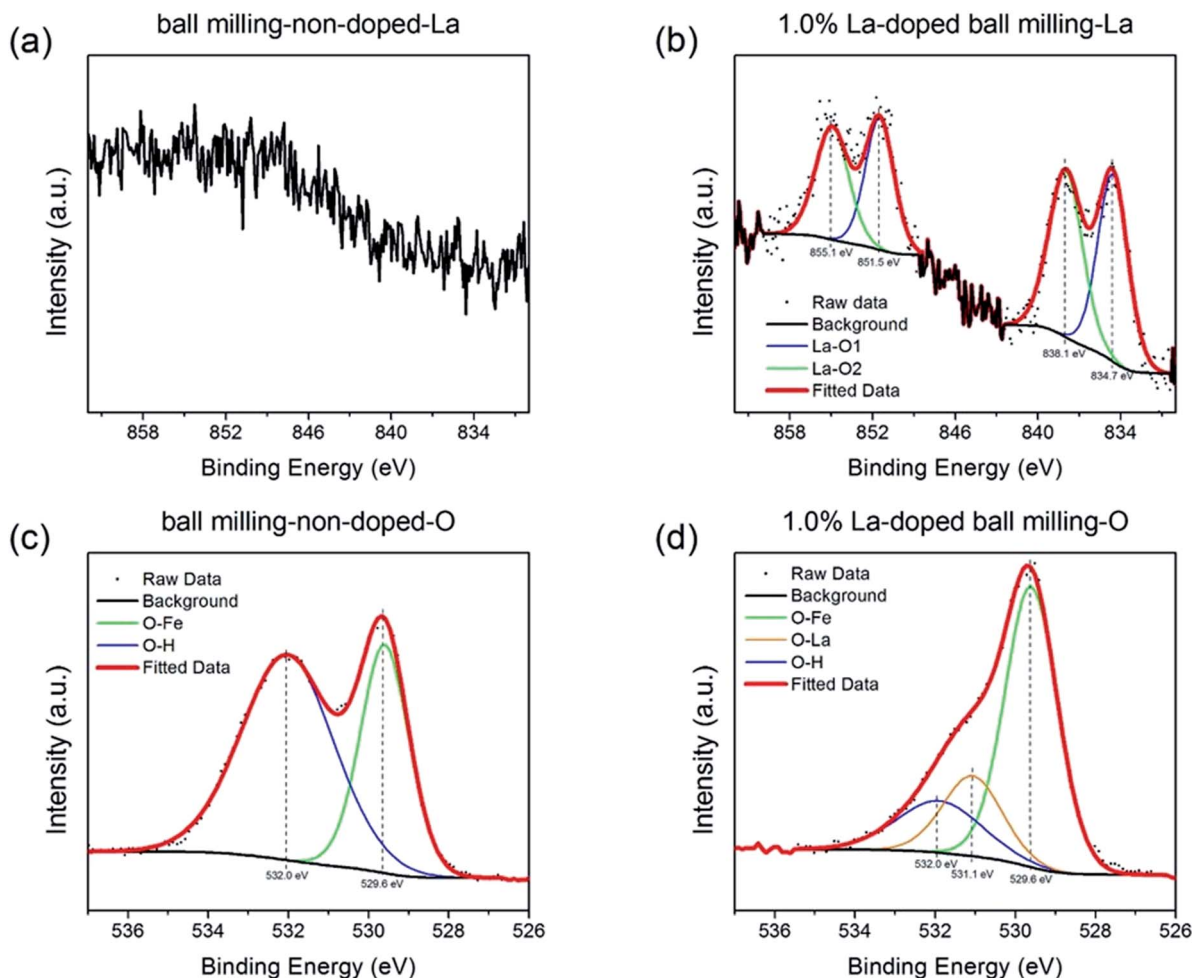


Fig. 2 XPS La 3d spectra of (a) undoped Fe_2O_3 and (b) 1% La-doped Fe_2O_3 . O 1s spectra of (c) undoped Fe_2O_3 and (d) 1% La-doped Fe_2O_3 .

that of undoped Fe_2O_3 . However, the reduction conversion rates of La-doped Fe_2O_3 oxygen carriers are lower than that of undoped oxygen carriers at 800 °C. As one can observe in Fig. 5, the surface of La-doped Fe_2O_3 has a less porous surface compared to undoped Fe_2O_3 at this higher temperature, indicating that the concentration of La is higher than 5% at the surface and the dopant serves as a sintering aid.²⁷ This explains the deteriorated reactivity of La-doped Fe_2O_3 at temperatures of 800 °C and above. The oxidation conversion rates of reduced oxygen carriers are also shown in Fig. 3(b), which represents the regeneration capability of oxygen carriers. With the same trend as that of the reduction reactions, reduced 1% La-doped Fe_2O_3 has more than two times higher conversion rates than Fe_2O_3 between 600 °C and

750 °C, with the maximal difference of 266% occurring at 700 °C. Similar to CO reduction, the oxygen regeneration conversion rates are lower in La-doped oxygen carriers at 800 °C, compared to undoped oxygen carriers. The average temperature dependent conversion rates are plotted in Fig. 4. Overall, based on the plot, an increase in reactivity is predicted to occur between 550 °C and 780 °C.

The recyclability of the oxygen carriers is also revealed from Fig. 3, and we can conclude that La-doped Fe_2O_3 has substantially better recyclability between 550 °C and 750 °C compared to undoped Fe_2O_3 . This observation is consistent with the morphological evolution of Fe_2O_3 and 1% La-doped Fe_2O_3 , which are imaged by SEM in Fig. 5(a) and (b). The average grain sizes in Fe_2O_3 and 1% La-doped Fe_2O_3 are 10 μm and 4 μm ,

Table 1 The distribution of different La or O species in Fe_2O_3 and La-doped Fe_2O_3

Sample	O 1s			La 3d		La/O
	O-H	O-La	O-Fe	La-O ₁	La-O ₂	
Fe_2O_3	63.15%	—	36.85%	—	—	—
1% La-doped Fe_2O_3	18.34%	20.02%	61.64%	50.47%	49.53%	0.054

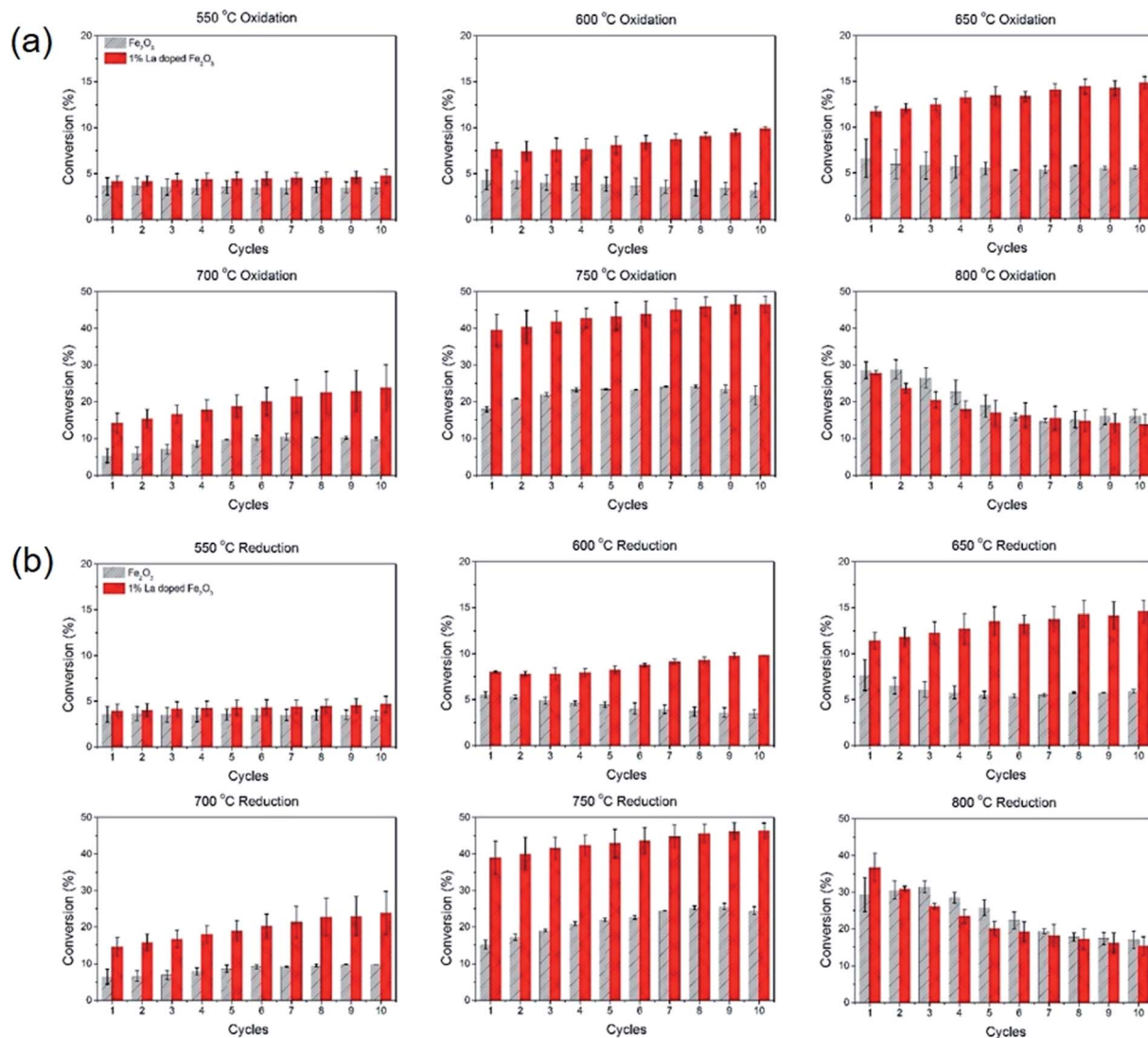


Fig. 3 Cyclic oxygen carrier conversion rate at 550–800 °C of (a) reduction and (b) oxidation regeneration.

respectively. The shrinkage of grain sizes in 1% La-doped Fe_2O_3 carriers is due to the fact that La^{3+} ions have a tendency to localize at grain boundaries, which inhibits grain growth.²⁸ After cyclic reduction reactions with CO, both undoped and La-doped Fe_2O_3 particles possess a porous surface. These pores are formed due to the outward diffusion of oxygen.^{1,29} Unlike aliovalent dopants that can create defects and promote ionic conductivity, La^{3+} is an isovalent dopant to Fe^{3+} , meaning that the La dopant cannot promote the formation of a defective surface in Fe_2O_3 . In Fig. 5, we can also compare the surface morphology of undoped and doped Fe_2O_3 oxygen carriers before and after cyclic reactions. Clearly, the addition of La dopants decreases the grain size of Fe_2O_3 , which in turn increases the surface area and promotes the reactivity and recyclability of the oxygen carriers. At lower temperatures in the 550–780 °C range, sintering promoted by La dopants only plays a minor role; thus the La-doped Fe_2O_3 demonstrates stable recyclability during the redox reactions. In contrast, at a higher

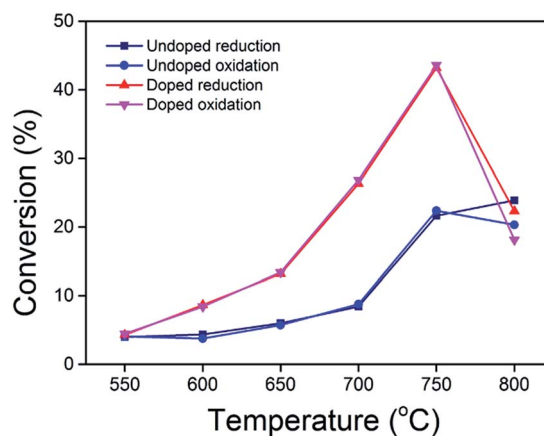


Fig. 4 Average conversion–temperature relationship of doped and undoped iron oxide oxygen carriers.

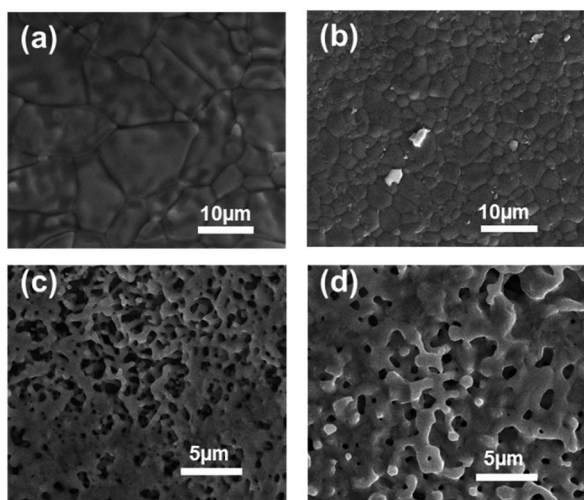


Fig. 5 SEM images of (a) initial Fe_2O_3 microparticles, (b) initial La-doped Fe_2O_3 microparticles, (c) reduced Fe_2O_3 microparticles after cyclic redox reactions at 800°C , and (d) reduced La-doped Fe_2O_3 microparticles after cyclic redox reactions at 800°C .

temperature of 800°C and above, the CO reduction rate of La-doped iron oxide is lower than that of undoped iron oxide, indicating the La-dopant promoted sintering plays a major role at higher temperatures.

To gain mechanistic insight into the role of low La-dopant concentrations in the reactivity of Fe_2O_3 for CO conversion, we first studied CO adsorption on a La-doped Fe_2O_3 surface using DFT calculations. We model the surface using an Fe_2O_3 (001) slab because the Fe_2O_3 (001) surface orientation is dominant, as shown in X-ray photoelectron diffraction studies.³⁰ Along the axis normal to the surface, the stacking sequence of hexagonal iron and lattice oxygen layers can be described as $\cdots\text{Fe}_{(1)}\text{-Fe}_{(2)}\text{-O}_3\text{-Fe}_{(1)}\text{-Fe}_{(2)}\text{-O}_3\cdots$. The Fe layer forms a $(\sqrt{3} \times \sqrt{3}) R30^\circ$ structure with respect to the close-packed

lattice oxygen layer, leading to an Fe-Fe distance of 5.035 \AA , which is the lattice constant of the Fe_2O_3 unit cell.

Based on surface free energy calculations for the Fe_2O_3 (001) surface with various termination types, we found that the $\text{Fe}_{(2)}\text{-O}_3\text{-Fe}_{(1)}\text{-Fe}_{(2)}\text{-O}_3\text{-Fe}_{(1)}\cdots$ termination is the most stable at 700°C .³¹ Therefore, substitutions were made at the slab with the $\text{Fe}_{(2)}\text{-O}_3\text{-Fe}_{(1)}\text{-Fe}_{(2)}\text{-O}_3\text{-Fe}_{(1)}\cdots$ termination. Using the first O_3 layer as the reference layer s , we replaced $\text{Fe}_{(2)}$ at the $s + 1$ layer with one La atom to build the doping system $\text{La-O}_3\text{-Fe}_{(1)}\text{-Fe}_{(2)}\cdots$. We then further used one La atom to replace $\text{Fe}_{(1)}$ at the $s - 1$ layer to build $\text{La-O}_3\text{-La-Fe}_{(2)}\cdots$ or $\text{Fe}_{(2)}$ at the $s - 2$ layer to build $\text{La-O}_3\text{-Fe}_{(1)}\text{-La}\cdots$. It was found that the surface free energy of $\text{La-O}_3\text{-Fe}_{(1)}\text{-Fe}_{(2)}\cdots$ is 1.39 J m^{-2} , which is 0.54 J m^{-2} lower than the surface free energies of $\text{La-O}_3\text{-La-Fe}_{(2)}\cdots$, and 0.68 J m^{-2} lower than the surface free energies of $\text{La-O}_3\text{-Fe}_{(1)}\text{-La}\cdots$. Therefore, $\text{La-O}_3\text{-Fe}_{(1)}\text{-Fe}_{(2)}\cdots$ is the dominant termination, which indicates that the La dopant prefers to migrate to the outermost layer of the iron oxide surface and that La dopant aggregation is not favorable.

CO adsorption on the $\alpha\text{-Fe}_2\text{O}_3$ (001) surface with the $\text{La-O}_3\text{-Fe}_{(1)}\text{-Fe}_{(2)}\cdots$ termination is done by considering five configurations of the CO molecule on the surface: the top site of the doped La atom (La atop); the top site of $\text{Fe}_{(1)}$ in the $s + 1$ layer (Fe atop); the top site of O in the s layer (O atop); the La-O bridging site (La-O bridge); and the $\text{Fe}_{(2)}\text{-O}$ bridging site (Fe-O bridge). These adsorption configurations are modeled, optimized and calculated.

In the “La atop” adsorption configuration (Fig. 6(a)), the CO molecule is perpendicularly chemisorbed on the surface, where the C atom of CO is bonded to the La atom with a distance of 1.926 \AA . In this case, the C-O bond of CO is activated and lengthened, which is 1.148 \AA in length and longer than that of CO in the gas phase (1.128 \AA). In the “Fe atop” adsorption configuration where $\text{Fe}_{(2)}$ is close to the La atom (Fig. 6(b)), the CO molecule also prefers to be perpendicularly chemisorbed,

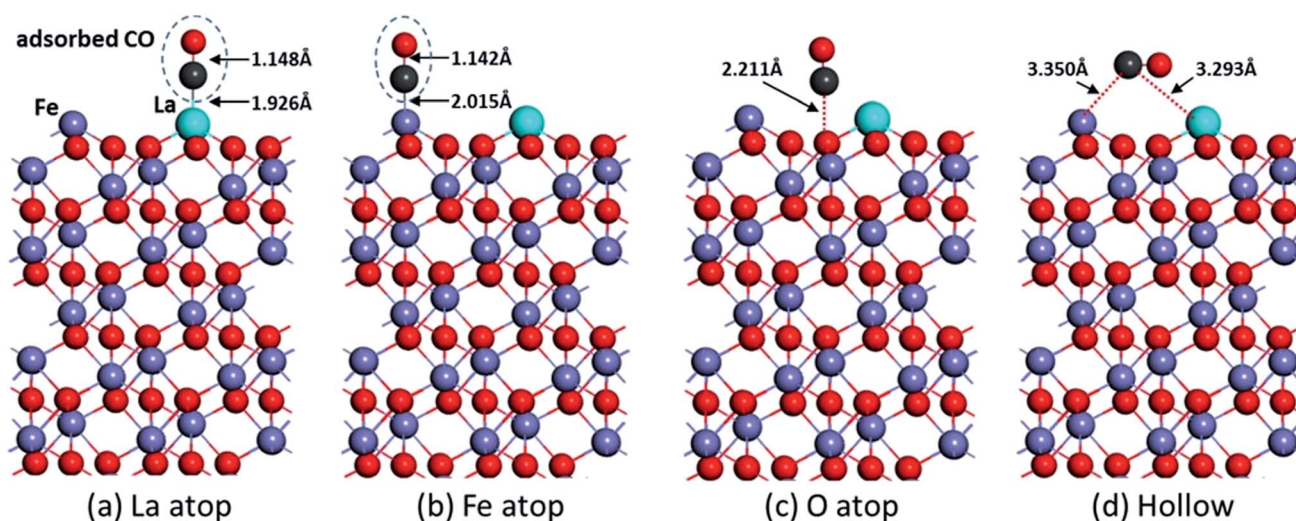


Fig. 6 CO adsorption configurations on a 1% La doped $\alpha\text{-Fe}_2\text{O}_3$ (001) surface. The CO bond length and the distance between the C atom and the closest surface atom are indicated.

Table 2 Representative structural parameters and energies of adsorption for a CO molecule adsorbed at various sites on the 1% La doped α -Fe₂O₃ (001) surface

Adsorption site	La atop	Fe atop	O atop site	La-O bridge	Fe-O bridge
Adsorption energy E_{ad} (eV)	0.872	0.785	0.155	0.532	0.465
C-O bond length (Å)	1.148	1.142	1.133	1.336	1.337

with a C-Fe distance of 2.015 Å and a C-O bond length of 1.142 Å.

Vertical adsorption at the “Fe-O bridge” site is less energetically favorable ($E_{\text{ads}} = 0.465$ eV) than for the “La-O bridge” site ($E_{\text{ads}} = 0.532$ eV). However, for the “O atop” site, the adsorption configuration is unstable since the CO molecule remains nearly physically unchanged upon adsorption and the distance between CO and the surface O is more than 2 Å, which is too far to form a new C-O bond (Fig. 6(c)). We also considered the hollow site adsorption and found that the CO molecule will be parallel to the surface without chemical bond formation after optimization (Fig. 6(d)). Overall, our calculations (Table 2) indicate that among the examined sites, only the “La atop” and “Fe atop” sites with neighboring La atoms are favorable for CO adsorption on the α -Fe₂O₃ (001) surface.

To take into consideration realistic experimental conditions (700 °C for CO oxidation), the effect of the temperature T is included by explicitly taking into account the surrounding gas phase in terms of *ab initio* atomistic thermodynamics. We previously developed a modified Brønsted-Evans-Polanyi relationship to calculate the activation energy for the elementary steps of metathesis reactions.³² Here, we used this method to

calculate the activation energy for CO oxidation on the 1% La-doped Fe₂O₃ surface under chemical looping conditions.

When CO is adsorbed to the “La atop” site of the 1% La-doped α -Fe₂O₃ (001) surface, the La-O bond length (1.93 Å) becomes a little longer than that of the clean surface (1.91 Å). The CO oxidation process initiated from the “La atop” adsorption configuration is depicted in Fig. 7. The C atom moves toward the saturated surface O atom neighboring the La dopant, and then pulls it out of the surface to form a new C-O bond. During this process, the O-La bond breaks with a barrier of 0.69 eV, which leads to CO₂ formation. When CO adsorbs to the “Fe atop” site, the oxidation involves an initial CO diffusion to form an unsymmetric bridged carbonate species. Then, the bidentate carbonate species is released from the surface and is accompanied by the formation of CO₂. The calculated barrier for this step is 1.035 eV. We see in the plot that 1% La reduces the energy barrier for CO oxidation on iron oxide to only 0.69 eV by the “La atop” pathway and 1.035 eV by the “Fe atop” pathway, compared to the 1.95 eV barrier from pristine Fe₂O₃.⁵

More generally, La-doped iron oxide oxygen carriers enhanced CO oxidation for differing reduction states of the iron oxide. Our experiments were carried out with a conversion of approximately 30% to avoid carbon deposition, which indicates that the iron oxides in our system only included Fe₂O₃, Fe₃O₄, and FeO phases. We further examined the effects of 1% La doping on Fe₃O₄ and FeO reactivity. 1% La-Fe₃O₄ has a cubic inverse spinel structure with a lattice constant of 8.402 Å (8.396 Å for Fe₃O₄). The O anions form a close-packed face-centered cubic (fcc) structure with Fe²⁺ and Fe³⁺ ions located in the interstitial sites. Based on this model, we calculated the CO activation energy and found that the barrier is 0.92 eV lower than that on undoped Fe₃O₄. Also, the barrier of CO oxidation on FeO is 0.85 eV lower than that on the undoped surface.

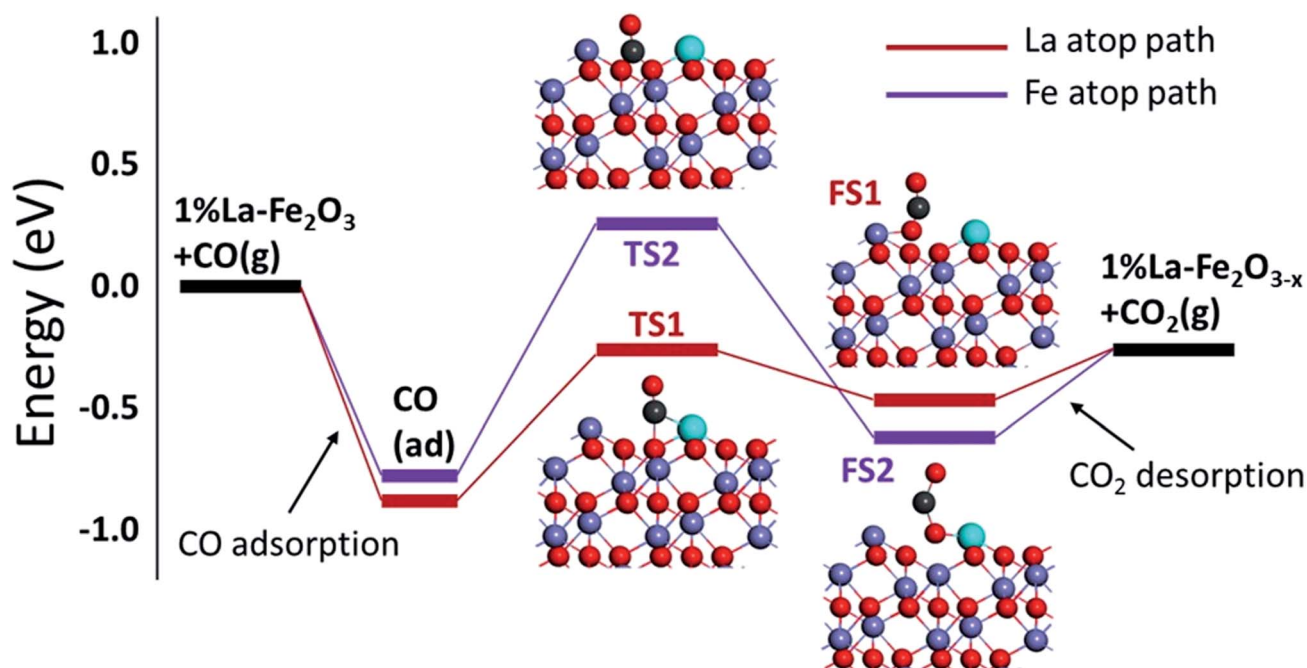


Fig. 7 The energy profile of CO oxidation on a 1% La-doped Fe₂O₃ surface.

Therefore, the 1% La dopant significantly reduced the barrier of CO oxidation on iron oxide oxygen carriers, which agrees with the reactivity improvement observed in our TGA experiments.

Conclusions

Very low concentration of isovalent (*e.g.*, La) and aliovalent (*e.g.*, Ni) metal oxide dopants to reduce the energy barrier of carbonaceous feedstock activation on metal oxide materials during the redox process and hence augmentation of the carbonaceous feedstock conversion was first initiated by Qin *et al.*^{5,17,18} In this study, low concentrations (1%) of lanthanum dopants in Fe₂O₃ oxygen carriers is found to dramatically promote CO reactivity, as well as oxygen carrier regeneration activity, while improving the recyclability of iron-based oxygen carriers. It is found that the reactivity of La-doped oxygen carriers is higher than that of undoped iron oxide oxygen carriers between 550 °C and 780 °C. The maximum reactivity increase happens at 700 °C, where the CO combustion reactivity increases by 233% and the air regeneration reactivity increases by 266%. The mechanism for the enhancement in La dopant-based reactivity stems from the ability of the La dopants to lower the barriers of the C–O bond activation during metal oxide redox reactions with CO. Our findings show how a dramatic modification in metal oxide oxygen carrier properties can be made using a relatively simple fabrication process, and we anticipate that this will impact future chemical looping particle design.

Acknowledgements

The valuable support provided by the Center for Electron Microscopy and the Analysis, and NanoSystem Laboratory at The Ohio State University and by the Supercomputer Center is gratefully acknowledged. The authors would like to thank OCRC for funding support (project No. R-14-09).

References

- 1 L. Qin, Z. Cheng, J. A. Fan, D. Kopechek, D. Xu, N. Deshpande and L.-S. Fan, *J. Mater. Chem. A*, 2015, **3**, 11302–11312.
- 2 X. Hua and W. J. Wang, *J. Environ. Sci.*, 2015, **32**, 135–145.
- 3 M. Ishida and H. Jin, *Ind. Eng. Chem. Res.*, 1996, **35**, 2469–2472.
- 4 L. Qin, Z. Cheng, M. Guo, J. A. Fan and L.-S. Fan, *Acta Mater.*, 2017, **124**, 568–578.
- 5 L. Qin, Z. Cheng, M. Guo, J. A. Fan and L.-S. Fan, *ACS Energy Lett.*, 2017, **2**, 70–74.
- 6 Y. Cao, S. P. Sit and W.-P. Pan, *Aerosol Air Qual. Res.*, 2014, **14**, 572–584.
- 7 Y. Cao, S. P. Sit and W.-P. Pan, *J. Therm. Anal. Calorim.*, 2014, **116**, 1257–1266.
- 8 T. Niu, G. L. Liu, Y. Chen, J. Yang, J. Wu, Y. Cao and Y. Liu, *Appl. Surf. Sci.*, 2016, **364**, 388–399.
- 9 S. A. Mohamed, M. R. Quddus, S. A. Razzak, M. M. Hossain and H. I. de Lasa, *Energy Fuels*, 2015, **29**, 6095–6103.
- 10 L. Liu and M. R. Zachariah, *Energy Fuels*, 2013, **27**, 4977–4983.
- 11 M. Wang, J. Liu, J. Hu and F. Liu, *Ind. Eng. Chem. Res.*, 2015, **54**, 9805–9812.
- 12 Q. Imtiaz, A. Kurlov, J. L. M. Rupp and C. R. Muller, *ChemSusChem*, 2015, 2055–2065.
- 13 A. Mishra, N. Galinsky, F. He, E. E. Santiso and F. Li, *Catal. Sci. Technol.*, 2016, **6**, 4535–4544.
- 14 L. M. Neal, A. Shafiearhood and F. Li, *ACS Catal.*, 2014, **4**, 3560–3569.
- 15 Z. Cheng, L. Qin, M. Guo, J. A. Fan, D. Xu and L.-S. Fan, *Phys. Chem. Chem. Phys.*, 2016, **18**, 16423–16435.
- 16 Z. Cheng, B. Sherman and C. Lo, *J. Chem. Phys.*, 2013, **138**, 014702.
- 17 L. Qin, Z. Cheng, M. Guo, M. Xu, J. A. Fan and L.-S. Fan, lecture, *ACS 252nd National Meeting & Exposition*, Philadelphia, PA, 2016.
- 18 L.-S. Fan, L. Qin, Z. Cheng and M. Guo, U. S. provisional patent No. 62/519, 376, 2017.
- 19 B. Li and H. Metiu, *J. Phys. Chem. C*, 2010, 12234–12244.
- 20 R. G. S. Pala, W. Tang, M. M. Sushchikh, J. N. Park, A. J. Forman, G. Wu, A. Kleiman-Shwarscstein, J. Zhang, E. W. McFarland and H. Metiu, *J. Catal.*, 2009, **266**, 50–58.
- 21 G. Kresse and J. Hafner, *Phys. Rev. B: Condens. Matter Mater. Phys.*, 1993, **47**, 558.
- 22 G. Kresse and J. Furthmuller, *Comput. Mater. Sci.*, 1996, **6**, 15.
- 23 G. Kresse and J. Furthmuller, *Phys. Rev. B: Condens. Matter Mater. Phys.*, 1996, **54**, 11169.
- 24 J. P. Perdew, K. Burke and M. Ernzerhof, *Phys. Rev. Lett.*, 1996, **77**, 3865.
- 25 A. Machocki, T. Ioannides, B. Stasinska, W. Gac, G. Avgouropoulos, D. Delimaris, W. Grzegorzczuk and S. Pasieczna, *J. Catal.*, 2004, **227**, 282–296.
- 26 E. McCafferty and J. P. Wightman, *Surf. Interface Anal.*, 1998, **26**, 549–564.
- 27 X. L. Li, H. A. Ma, Y. J. Zheng, Y. Liu, G. H. Zuo, W. Q. Liu, J. G. Li and X. Jia, *J. Alloys Compd.*, 2008, **463**, 412–416.
- 28 Ø. Johannesen and A. G. Andersen, *Selected Topics in High Temperature Chemistry: Defect Chemistry of Solids*, Elsevier, 1989.
- 29 L. Qin, A. Majumder, J. A. Fan, D. Kopechek and L.-S. Fan, *J. Mater. Chem. A*, 2014, **2**, 17511–17520.
- 30 R. L. Kurtz and V. E. Henrich, *Surf. Sci.*, 1983, **129**, 345–354.
- 31 Z. Cheng, L. Qin, M. Guo, M. Xu, J. A. Fan and L.-S. Fan, *Phys. Chem. Chem. Phys.*, 2016, **18**, 32418–32428.
- 32 Z. Cheng and C. S. Lo, *ACS Catal.*, 2015, **5**, 59–72.